MAGIC detection of GRB 201216C at z = 1.1

Author(s):
Abe, H.; Abe, S.; Acciari, V.A.; Agudo, I.; Aniello, T.; Ansoldi, S.; Antonelli, L.A.; Arbet Engels, A.; Arcaro, C.; Artero, M.; Asano, Katsuaki; Baack, D.; Babić, A.; Baquero, A.; Barres de Almeida, U.; Barrio, J.A.; Batković, I.; Baxter, J.; Becerra González, J.; Bednarek, W.; Biland, A.; Fukami, Satoshi; et al.

Publication date:
2024-01

Permanent link:
https://doi.org/10.3929/ethz-b-000649833

Originally published in:
Monthly Notices of the Royal Astronomical Society 527(3), https://doi.org/10.1093/mnras/stad2958

Monthly Notices of the ROYAL ASTRONOMICAL SOCIETY

MNRAS **527,** 5856–5867 (2024) https://doi.org/10.1093/mnras/stad2958
Advance Access publication 2023 October 23

MAGIC detection of GRB 201216C at $z = 1.1$

H. Abe,[1] S. Abe,[1] V. A. Acciari,[2] I. Agudo,[3] T. Aniello,[4] S. Ansoldi,[5,6] L. A. Antonelli,[4] A. Arbet Engels,[7] C. Arcaro,[8] M. Artero,[9] K. Asano,[1] D. Baack,[10] A. Babić,[11] A. Baquero,[12] U. Barres de Almeida,[13] J. A. Barrio,[12] I. Batković,[8] J. Baxter,[1] J. Becerra González,[2] W. Bednarek,[14] E. Bernardini,[8] J. Bernete,[15] A. Berti,[7]★ J. Besenrieder,[7] C. Bigongiari,[4] A. Biland,[16] O. Blanch,[9] G. Bonnoli,[4] Ž. Bošnjak,[11] I. Burelli,[5] G. Busetto,[8] A. Campoy-Ordaz,[17] A. Carosi,[4] R. Carosi,[18] M. Carretero-Castrillo,[19] A. J. Castro-Tirado,[3] G. Ceribella,[7] Y. Chai,[7] A. Cifuentes,[15] S. Cikota,[11] E. Colombo,[2] J. L. Contreras,[12] J. Cortina,[15] S. Covino,[4] G. D'Amico,[20] V. D'Elia,[4] P. Da Vela,[18,21] F. Dazzi,[4] A. De Angelis,[8] B. De Lotto,[5] A. Del Popolo,[22] M. Delfino,[9,23] J. Delgado,[9,23] C. Delgado Mendez,[15] D. Depaoli,[24] F. Di Pierro,[24] L. Di Venere,[25] D. Dominis Prester,[26] A. Donini,[4] D. Dorner,[27] M. Doro,[8] D. Elsaesser,[10] G. Emery,[28] J. Escudero,[3] L. Fariña,[9] A. Fattorini,[10] L. Foffano,[4] L. Font,[17] S. Fukami,[16]★ Y. Fukazawa,[29] R. J. García López,[2] M. Garczarczyk,[30] S. Gasparyan,[31] M. Gaug,[17] J. G. Giesbrecht Paiva,[13] N. Giglietto,[25] F. Giordano,[25] P. Gliwny,[14] N. Godinović,[32] R. Grau,[9] D. Green,[7] J. G. Green,[7] D. Hadasch,[1] A. Hahn,[7] T. Hassan,[15] L. Heckmann,[7,33] J. Herrera,[2] D. Hrupec,[34] M. Hütten,[1] R. Imazawa,[29] T. Inada,[1] R. Iotov,[27] K. Ishio,[14] I. Jiménez Martínez,[15] J. Jormanainen,[35] D. Kerszberg,[9] G. W. Kluge,[20,36] Y. Kobayashi,[1] P. M. Kouch,[35] H. Kubo,[1] J. Kushida,[37] M. Láinez Lezáun,[12] A. Lamastra,[4] F. Leone,[4] E. Lindfors,[35] L. Linhoff,[10] S. Lombardi,[4] F. Longo,[5,38] R. López-Coto,[3] M. López-Moya,[12] A. López-Oramas,[2] S. Loporchio,[25]★ A. Lorini,[39] E. Lyard,[28] B. Machado de Oliveira Fraga,[13] P. Majumdar,[40] M. Makariev,[41] G. Maneva,[41] N. Mang,[10] M. Manganaro,[26] S. Mangano,[15] K. Mannheim,[27] M. Mariotti,[8] M. Martínez,[9] A. Mas-Aguilar,[12] D. Mazin,[1,7] S. Menchiari,[39] S. Mender,[10] S. Mićanović,[26] D. Miceli,[8] T. Miener,[12] J. M. Miranda,[39] R. Mirzoyan,[7] M. Molero González,[2] E. Molina,[2] H. A. Mondal,[40] A. Moralejo,[9] D. Morcuende,[12] C. Nanci,[4] L. Nava,[4]★ V. Neustroev,[42] M. Nievas Rosillo,[2] C. Nigro,[9] L. Nikolić,[39] K. Nilsson,[35] K. Nishijima,[37] T. Njoh Ekoume,[2] K. Noda,[43] S. Nozaki,[7] Y. Ohtani,[1] A. Okumura,[44] J. Otero-Santos,[2] S. Paiano,[4] M. Palatiello,[5] D. Paneque,[7] R. Paoletti,[39] J. M. Paredes,[19] L. Pavletić,[26] D. Pavlović,[26] M. Persic,[5,45] M. Pihet,[8] G. Pirola,[7] F. Podobnik,[39] P. G. Prada Moroni,[18] E. Prandini,[8] G. Principe,[5] C. Priyadarshi,[9] W. Rhode,[10] M. Ribó,[19] J. Rico,[9] C. Righi,[4] N. Sahakyan,[31] T. Saito,[1] K. Satalecka,[35] F. G. Saturni,[4] B. Schleicher,[27] K. Schmidt,[10] F. Schmuckermaier,[7] J. L. Schubert,[10] T. Schweizer,[7] A. Sciaccaluga,[4] J. Sitarek,[14] V. Sliusar,[28] D. Sobczynska,[14] A. Spolon,[8] A. Stamerra,[4] J. Strišković,[34] D. Strom,[7] M. Strzys,[1] Y. Suda,[29]★ S. Suutarinen,[35] H. Tajima,[44] M. Takahashi,[44] R. Takeishi,[1] F. Tavecchio,[4] P. Temnikov,[41] K. Terauchi,[46] T. Terzić,[26] M. Teshima,[1,7] L. Tosti,[47] S. Truzzi,[39] A. Tutone,[4] S. Ubach,[17] J. van Scherpenberg,[7] M. Vazquez Acosta,[2] S. Ventura,[39] V. Verguilov,[41] I. Viale,[8] C. F. Vigorito,[24] V. Vitale,[48] I. Vovk,[1] R. Walter,[28] M. Will,[7] T. Yamamoto,[49] A. Gomboc,[50] N. Jordana-Mitjans,[51] A. Melandri,[4,52] C. G. Mundell,[51,53] M. Shrestha[54,55] and I. A. Steele[54]

Affiliations are listed at the end of the paper

Accepted 2023 September 22. Received 2023 September 18; in original form 2023 June 15

★ E-mail: contact.magic@mpp.mpg.de

ABSTRACT

Gamma-ray bursts (GRBs) are explosive transient events occurring at cosmological distances, releasing a large amount of energy as electromagnetic radiation over several energy bands. We report the detection of the long GRB 201216C by the MAGIC telescopes. The source is located at $z = 1.1$ and thus it is the farthest one detected at very high energies. The emission above 70 GeV of GRB 201216C is modelled together with multiwavelength data within a synchrotron and synchrotron self-Compton (SSC) scenario. We find that SSC can explain the broad-band data well from the optical to the very-high-energy band. For the late-time radio data, a different component is needed to account for the observed emission. Differently from previous GRBs detected in the very-high-energy range, the model for GRB 201216C strongly favours a wind-like medium. The model parameters have values similar to those found in past studies of the afterglows of GRBs detected up to GeV energies.

Key words: astroparticle physics – radiation mechanisms: non-thermal – gamma-ray burst: individual: GRB 201216C – gamma-ray bursts.

1 INTRODUCTION

Gamma-ray bursts (GRBs) are sources exhibiting bright electromagnetic emission in two phases called *prompt* and *afterglow*. The former peaks at hard X-ray and soft gamma-ray energies, lasting between a fraction of a second and hundreds of seconds. In particular, the prompt temporal behaviour shows short time-scale variability down to milliseconds. Although its origin is not completely understood (for a review, see Kumar & Zhang 2015), recent evidence is pointing to a synchrotron origin (Zhao et al. 2014; Zhang et al. 2016; Oganesyan et al. 2017, 2018, 2019). The afterglow radiation partly overlaps with the prompt and evolves over longer time-scales, up to several months after the GRB onset. The emission in this phase decays smoothly with time as a power law and it can be detected in several energy bands, from radio up to gamma rays, and is interpreted as synchrotron and Inverse Compton emission mostly from electrons accelerated in the external shock (Sari, Piran & Narayan 1998; Panaitescu & Kumar 2000).

GRBs are classified as short and long depending on whether their duration in terms of T_{90}, the time interval containing 90 per cent of the total photon counts, is shorter or longer than two seconds. While this observational definition is widely adopted, a more physical classification comes from the progenitor system at the origin of the bursts. In this context, short GRBs are thought to be produced as the result of the merger of binary systems of compact objects involving at least one neutron star (NS). The only confirmation of such association is the short GRB 170817A, which was detected in coincidence with a gravitational wave signal generated by a NS–NS merger (Abbott et al. 2017; Goldstein et al. 2017). Alternatively, long GRBs are often associated with Type Ib/c, when detectable (e.g. if redshift is $z \lesssim 1$). The supernova emission peaks several days after the GRB onset, when it outshines the decaying optical afterglow of the burst itself (Woosley & Bloom 2006).

The afterglow phase of GRBs has been studied in detail over several wavelength bands thanks to numerous instruments both ground based (covering the radio and optical wavelengths and VHE gamma rays) and space based (detecting X-rays and gamma rays). Such observations have made it possible to trace the origin of the multiwavelength afterglow emission to the synchrotron process (Mészáros 2002; Piran 2004). Such radiation is mostly produced by electrons accelerated at the so-called forward shock, when the GRB jet decelerates by interacting with the interstellar or circumstellar medium. Until recently, the afterglow was detected up to GeV energies by the *Fermi*-LAT instrument, with some hints of a possible tail extending to higher energies (Ackermann et al. 2014), where imaging atmospheric Cherenkov telescopes (IACTs) are more sensitive. The presence of emission in the very-high-energy (VHE, $E > 100$ GeV) range in the afterglow phase of GRBs was predicted, even before the operation of *Fermi*-LAT and IACTs, in several theoretical models involving either leptonic or hadronic processes. A breakthrough was achieved in 2019, when the detection of VHE emission in the afterglow of three long GRBs was reported. The MAGIC collaboration first reported the detection of GRB 190114C (Mirzoyan et al. 2019; MAGIC Collaboration et al. 2019a, b), followed by GRB 180720B and GRB 190829A detected by the H.E.S.S. telescopes (Abdalla et al. 2019; H. E. S. S. Collaboration et al. 2021). The detection of such sources with IACTs confirmed the presence of an emission in the VHE range. In particular, the spectral and temporal analysis of GRB 190114C showed that such emission is associated with a component, separate from the synchrotron one, well explained by synchrotron self-Compton (SSC) radiation from electrons accelerated at the forward shock. A similar conclusion can be drawn for GRB 180720B (see e.g. Wang et al. 2019), even though the multiwavelength data available were not enough to perform a proper modelling. An unusual and controversial interpretation was put forward in the case of GRB 190829A. In H. E. S. S. Collaboration et al. (2021) the authors suggested that the emission could be attributed to a single synchrotron component, which extends over nine orders of magnitude in energy up to the TeV domain. This requires an acceleration mechanism that is able to overcome the limit resulting in the so-called *burnoff limit* for the energy of synchrotron photons (de Jager et al. 1996; Piran & Nakar 2010).

The studies on this small sample of events shows how the understanding of the afterglow phase in the VHE range is far from complete. Currently only a few events have a detection at VHE (or evidence, as in GRB 160821B, see Acciari et al. 2021), and different interpretations were proposed. However, the SSC scenario proved to be flexible and applicable to all the three GRBs detected at VHE. In order to investigate if such an interpretation may be universal to explain VHE afterglows, we present here the detection of the long GRB 201216C with the MAGIC telescopes. We use the available multiwavelength data to model the broad-band emission in the SSC scenario. We find that the SSC model provides a satisfactory interpretation of the MAGIC light curve and spectrum.

The paper is organized as follows. In Section 2, we summarize all the observations available for GRB 201216C. In Section 3 we discuss the MAGIC observations and data analysis. The results are presented in Section 4. In Section 5, we present the analysis of optical observations taken with the Liverpool Telescope (LT) and the other multiwavelength observations that we use to model the emission with a synchrotron and SSC scenario (discussed in Section 6). Finally, in Section 7 we summarize and discuss our findings.

2 OBSERVATIONS OF GRB 201216C

GRB 201216C was detected by *Swift*-BAT on 2020 December 16 at 23:07:31 UT (Beardmore et al. 2020)[1], hereafter T_0. The burst was also detected by other space-based instruments including *Fermi*-GBM, ASTROSAT, and Konus-Wind. The light curve by *Swift*-BAT shows a multipeaked structure[2] from $T_0 - 16$ s to $T_0 + 64$ s, with a main peak occurring at $\sim T_0 + 20$ s.

GRB 201216C is classified as a long GRB, with a T_{90} estimated to 48(16) s in the $15 - 350$ keV band (*Swift*-BAT, Ukwatta et al. (2020)) and 29.953(572) s in the $50 - 300$ keV band (*Fermi*-GBM, Malacaria et al. 2020). The burst fluence in the $10 - 1000$ keV energy range between $T_0 - 0.003$ s to $T_0 + 49.665$ s is $1.41(6)e-4$ erg/ cm^2 . The 1-s peak photon flux measured starting from $T_0 + 24.8$ s in the same energy band is 54.9(6) phs^{-1}/ cm^2 .

Observations at different times by the VLT, FRAM-ORM, and the LT confirmed the presence of the optical afterglow. The position of the optical counterpart is consistent with the refined position provided by *Swift*-XRT. VLT X-Shooter spectroscopy at $\sim T_0 +$ 2.4 h, covering the wavelength range 3200–22 000 Å;, allowed the measurement of the redshift, estimated[3] to be $z = 1.1$. Based on the VLT photometry, the steep photon index of optical data suggests a significant extinction, making GRB 201216C a dark GRB (Vielfaure et al. 2020).

Assuming $z = 1.1$, the isotropic energy release and peak luminosity of GRB 201216C in the $20 - 10000$ keV energy range are $E_{\mathrm{iso},\gamma} = 6.2(6)e53$ erg and $L_{\mathrm{iso}} = 1.3(1)e53$ ergs^{-1}. With a rest-frame spectral peak energy of 685 ± 15 keV (Malacaria et al. 2020), GRB 201216C is consistent both with the Amati and Yonetoku correlations (Amati et al. 2002; Yonetoku et al. 2004).

The afterglow was also detected in the X-ray band by *Swift*-XRT. The X-ray afterglow decay[4] can be described as a power law with temporal index $\alpha = 1.75(9)$.

In the high-energy range (0.1–1 GeV), *Fermi*-LAT observed the burst from $T_0 + 3500$ s to $T_0 + 5500$ s but it did not detect any significant gamma-ray emission in such time interval, placing an energy flux upper limit of 3×10^{-10} erg/ cm^2 s^{-1} (95 per cent confidence level, $100\,\mathrm{MeV} < E < 1\,\mathrm{GeV}$, see Bissaldi et al. 2020).

At higher energies, the burst was observed by HAWC starting at $T_0 + 100$ s up to $T_0 + 3600$ s, resulting in a non-significant detection (Ayala 2020).

Detection of radio emission was reported by Rhodes et al. (2022) from 5 to 56 d after the burst, from 1 to 10 GHz. The radio flux at the time of detection is already decaying, although at a slow rate, except for the flux at 1 GHz, for which the flux is increasing between 30 and 40 d.

Finally, the burst was observed by the MAGIC telescopes in the VHE range. Details of such observations are given in the following section.

3 MAGIC OBSERVATION AND DATA ANALYSIS

MAGIC is a stereoscopic system of two 17-m diameter IACTs situated at the Observatory Roque de los Muchachos (ORM), La Palma, Canary Islands. For short observations, as the ones usually performed for GRBs, the integral sensitivity achieved by MAGIC in 20 min is about 20 per cent of the Crab Nebula flux above 105 GeV for low zenith angles (see Aleksić et al. 2016 for details on the telescopes performance).

MAGIC received the alert for GRB 201216C at 23:07:51 UT ($T_0 + 20$ s) from the *Swift*-BAT instrument. The MAGIC telescopes automatically reacted to the alert and, after a fast movement, they reached the target at 23:08:27 UT ($T_0 + 56$ s). The observation was carried out in the so-called wobble mode around the coordinates provided by *Swift*-BAT, RA: $01^{\mathrm{h}}05^{\mathrm{m}}26^{\mathrm{s}}$ Dec.: $+16^\circ32'12''$ (J2000). In local coordinates, the observation started at zenith 37.1°, lasting up to 01:30:08 UT reaching zenith 68.3°. The weather conditions were very good and stable during all the data taking with a median atmospheric transmission value at 9 km AGL from LIDAR measurements of 0.96, with 1 being the transmission of a clear atmosphere (see Fruck et al. 2022; Schmuckermaier et al. 2023 for a description of the LIDAR instrument and correction of VHE data). The observation was performed under dark conditions.

MAGIC continued the observation on the second night for 4.1 h from $T_0 + 73.8$ ks. The observational conditions were optimal with an average transmission above 0.9 at 9 km and dark conditions. The zenith angle changed from 17.0° to 46.3° with culmination at 11.7°. The data on the second night were taken with the analogue trigger system Sum-Trigger-II (described in Dazzi et al. 2021), which was not available during the first night of data taking. Sum-Trigger-II improves the sensitivity of MAGIC in the low-energy range below ∼100 GeV. In particular, the trigger efficiency, compared to the standard digital trigger, is two times larger for Sum-Trigger-II at 40 GeV.

The data analysis is performed using the standard MAGIC Reconstruction Software (MARS; Zanin et al. 2013). In order to retain as many low-energy events as possible, an algorithm (Shayduk 2013; MAGIC Collaboration et al. 2020) where the calibration and the image cleaning are performed in an iterative procedure was adopted. This image cleaning was applied to the GRB data, gamma-ray Monte Carlo data, and to a data sample taken on sky regions without any gamma-ray emission (used for the training of the particle identification algorithm). Data analysis beyond this level is performed following the prescriptions described in Aleksić et al. (2016). The usage of Sum-Trigger-II, combined with the optimized cleaning algorithm, allows for a collection area an order of magnitude larger around 20 GeV when compared with the one obtained with the standard digital trigger.

4 RESULTS FROM THE VHE DATA

In this section, we show the results of the analysis performed on the data collected by MAGIC on GRB 201216C.

4.1 Detection and sky map

Fig. 1 shows the distribution of the squared angular distance, θ^2, for the GRB and background events (red circles and blue squares, respectively) for the first 20 min of data (from $T_0 + 56$ s to $T_0 + 1224$ s). The significance of the VHE gamma-ray signal from GRB 201216C is 6.0σ, following the prescription of Li & Ma (1983), confirming the significant detection of the GRB. For the computation of the significance, we apply cuts on θ^2 and hadronness. The former is the squared angular distance between the reconstructed direction of the events and the nominal position of the source, taken from *Swift*-BAT for GRB 201216C. The latter is a parameter which discriminates between gamma-like and background-like events, with

[1]full GCN Circulars history at https://gcn.gsfc.nasa.gov/other/201216C.gcn3.
[2]see https://gcn.gsfc.nasa.gov/notices_s/1013243/BA/#lc.
[3]The value has been confirmed by the STARGATE collaboration via private communication.
[4]see https://www.swift.ac.uk/xrt_live_cat/01013243/.

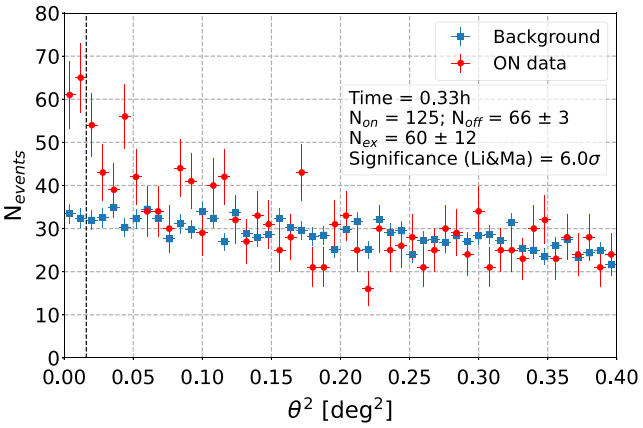

Figure 1. θ^2 distribution for the first 20 min of observation, see the main text for the definition. Both GRB (red circles) and background events (blue squares) are shown. The vertical dashed black line shows the value of the cut in θ^2 used for the calculation of the significance.

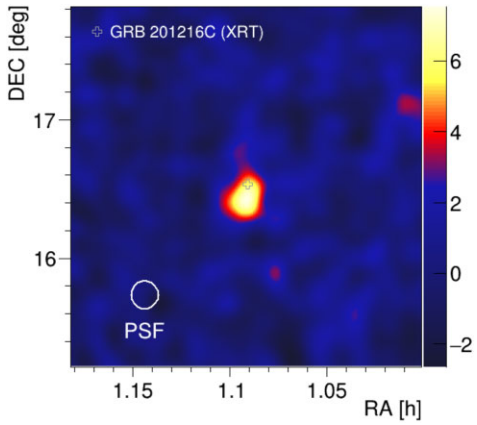

Figure 2. Test-statistics sky map for the first 20 min of observation. The cross marker shows the position of GRB 201216C reported by *Swift*-XRT. The white circle shows the MAGIC point spread function corresponding to 68 per cent containment.

gamma rays having hadronness values close to zero. The cuts on θ^2 and hadronness were optimized for a source with an intrinsic power-law spectrum with index $\alpha = -2$, later corrected considering the absorption by the extragalactic background light (EBL) according to the model by Domínguez et al. (2011), hereafter D11. For the signal significance evaluation, the intrinsic spectral index for the cut optimization was chosen to be similar to the one found in the other GRBs detected at VHE, so without any prior knowledge of the actual value for this specific GRB (see Section 4.2). The corresponding energy threshold of the optimized cuts is 80 GeV defined by the peak of the energy distribution of the surviving simulated events.

Fig. 2 shows the test-statistics map in sky coordinates for the first 20 min of data. The same event cuts as for Fig. 1 are used. Our test statistic is Li & Ma (1983) equation (17), applied on a smoothed and modelled background estimation. Its null hypothesis distribution mostly resembles a Gaussian function, but in general can have a somewhat different shape or width. In the sky map, the peak position around the center is consistent with the one reported by *Swift*-XRT within the statistical error. The peak significance is above 6σ, which corroborates the detection.

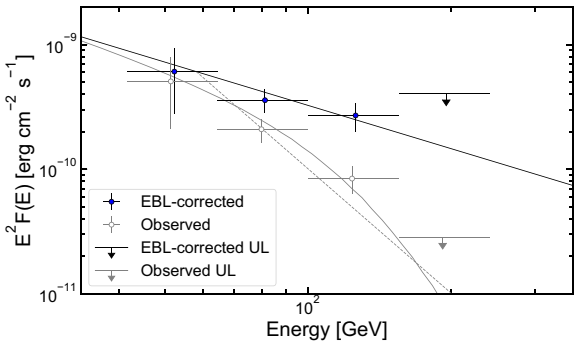

Figure 3. Observed and EBL-corrected spectra for GRB 201216C as measured by the MAGIC telescopes during the first 20 min of observations, denoted by white and blue filled points, respectively. The highest energy bin is a 2σ upper limit in each spectrum. The solid black and dashed grey lines represent the forward folding fits to the data points. The solid grey line is obtained from the intrinsic spectrum fit (black solid line) after the absorption by the EBL is taken into account, using the D11 model.

Table 1. Fitted power-law spectral parameters of the 20-min average spectrum using different scales of the Cherenkov light amount and different EBL models. The tested EBL models are D11, F08, FI10, and G12 with the nominal light scale. The tested light scales are nominal, −15 per cent, +15 per cent with the D11 EBL model. The normalization energy is fixed to 100 GeV. The errors are statistical only. The resulting systematic errors are reported in the main text.

Light scale	EBL	Normalization [TeV^{-1} cm^{-2} s^{-1}]	Index
Nominal	D11	2.03 ± 10^{-8}	-3.15 ± 0.70
−15 per cent	D11	1.14 ± 10^{-8}	-3.19 ± 0.52
+15 per cent	D11	2.99 ± 10^{-8}	-2.17 ± 0.57
Nominal	F08	1.95 ± 10^{-8}	-3.19 ± 0.70
Nominal	FI10	2.76 ± 10^{-8}	-2.65 ± 0.73
Nominal	G12	3.99 ± 10^{-8}	-2.45 ± 0.71

4.2 Average spectrum

The average spectrum for the first 20 min of observation is shown in Fig. 3. The data points are the result of an unfolding procedure following the prescription of the Bertero method described in Albert et al. (2007). The best fit to the points is instead provided by the forward folding method (Piron et al. 2001). For the event cuts optimization, the adopted spectrum is an intrinsic power-law spectrum with an index $\alpha = -3$, which is close to the final estimated value (see further), later attenuated by EBL assuming the model D11 and $z = 1.1$. Because of the strong EBL absorption, the observed spectrum has a steep power-law index of -5.32 ± 0.53 (stat. only) above 50 GeV. The intrinsic (EBL-corrected) spectrum is consistent with a simple power-law function and shows a harder index of -3.15 ± 0.70 (stat. only). The normalization factor at 100 GeV is 2.03 ± 10^{-8} TeV^{-1} cm^{-2} s^{-1} (stat. only). The highest energy bin around 200 GeV is a 2σ upper limit due to a large relative flux error about 100 per cent.

The obtained spectrum suffers from systematic uncertainties coming from different sources. For such a steep observed spectrum, the uncertainty of the energy scale significantly affects the computed fluxes. We estimated the flux variation by shifting the light scale in the simulations during the forward folding procedure assuming the EBL model D11. We adopted a ±15 per cent shift as prescribed in Aleksić et al. (2016). The results are shown in Table 1. When the energy

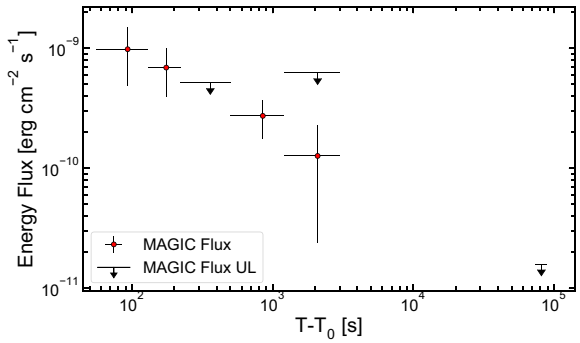

Figure 4. EBL-corrected energy-flux light curve between 70 and 200 GeV from T_0 +56 s to T_0 +40 min (first night, divided into five time bins) and from T_0 +20.5 h to T_0 +24.6 h (second night). Upper limits are calculated as 95 per cent confidence level for the bins with relative errors >50 per cent.

scale is shifted by –15 per cent, the observed spectrum is shifted to the low-energy side resulting in a lower flux. The spectral index of the intrinsic spectrum is softened due to the smaller attenuation by EBL at lower energies. In case of the +15 per cent shift, the flux and the spectral index are shifted in the opposite direction. The obtained power-law index ranges from –3.19 in the –15 per cent case to –2.17 in the +15 per cent case. The normalization factor instead varies by a factor of 3. The spectral uncertainty originating from the energy scale is therefore significantly larger than the statistical errors.

The VHE flux of GRB 201216C is also affected by the choice between available EBL models. At such high redhift $z = 1.1$, EBL models show large differences in predicted attenuation factors. We compared the spectra calculated with four EBL models including D11 with the same unfolding method as the one used for Fig. 3. The three models besides D11 are Franceschini, Rodighiero & Vaccari (2008), Finke, Razzaque & Dermer (2010), and Gilmore et al. (2012) (hereafter F08, FI10, and G12, respectively). The results are shown in Table 1. The power-law index ranges from –3.19 in the F08 case to –2.45 in the G12 case, and the normalization factor varies by a factor of 2. Also in this case, the systematic uncertainty on the parameters due to the EBL models is larger than or equal to the statistical errors.

At $z = 1.1$, D11 and F08 have similar attenuation values below 200 GeV, which is the maximum energy in our analysis. The attenuation discrepancy between D11 and G12 is a factor of 2 at 100 GeV and a factor of 5 at 200 GeV. Thus, the intrinsic spectrum has a larger normalization and it is harder in the G12 case than in the D11 and F08 case, as seen in Table 1.

The spectral index and normalization factor including the systematic uncertainties discussed earlier are therefore $-3.15^{+0.70}_{-0.70}(\mathrm{stat})^{+0.98}_{-0.04}(\mathrm{sys})^{+0.70}_{-0.04}(\mathrm{sysEBL})$ and $2.03^{+0.39}_{-0.39}(\mathrm{stat})^{+0.96}_{-0.89}(\mathrm{sys})^{+1.96}_{-0.08}(\mathrm{sysEBL}) \times 10^{-8}\,\mathrm{TeV^{-1}s^{-1}\,cm^{-2}}$, respectively. There are other systematic effects that may affect the spectral parameters (e.g. pointing accuracy and background uncertainty), as described in Aleksić et al. (2016), however they are ignored in the analysis because they are less relevant than the aforementioned ones.

4.3 Light curve

The VHE energy-flux light curve between 70 and 200 GeV is shown in Fig. 4. The energy flux of each time bin is obtained by integrating the EBL-corrected forward-folded spectrum with the D11 model, so that the spectral variability with time is taken into account. For each time bin, the event cut is based on the signal survival fraction of simulated events in order to increase the statistics in such short-time bins. The corresponding energy threshold is around 70 GeV for all the time bins. The light curve is compatible with a power-law decay. The best fit decay index until the 5th bin excluding upper limits is -0.62 ± 0.04.

Upper limits are calculated for bins where relative flux errors are larger than 50 per cent using the method described in (Rolke & López 2001). The excess count upper limit of 95 per cent confidence interval is calculated for each of such bins and converted into the energy flux unit by assuming the power-law spectrum with an index of –3 attenuated with the D11 model.

The systematic uncertainties considered in Section 4.2 also affect the flux points in the light curve to a similar extent. However, since the spectral shape is not expected to change significantly during the short period of each bin of the light curve, the relative flux error is similar among all the bins. Therefore, the temporal decay index should be independent of the uncertainties as long as the spectrum is assumed to be stable. In fact, we could not detect any significant spectral changes larger than the statistical error during the time interval where the light curve was produced.

From the analysis of the data on the second night, which spans from T_0 +20.5 h to T_0 +24.6 h, we found no significant excess around the position of the GRB with both the cut used in Section 4.1 and a conventional cut optimized for the Crab Nebula.

We calculated the flux upper limit on the second night assuming an intrinsic power-law spectrum with an index of –3 and the EBL model D11. The event cut applied is the same one as used for the light curve on the first night. The upper limit of the EBL-corrected flux is shown in Fig. 4. We note that the VHE luminosity of GRB 201216C implied by MAGIC observations is fainter (a factor 10–30) than the luminosity predicted by Zhang et al. (2023) on the basis of their afterglow modelling at lower frequencies.

5 MULTIWAVELENGTH DATA FROM RADIO TO GAMMA-RAY

In this Section, we give an overview of the data at lower energies collected from the literature or analysed in this work, and later used for modelling and interpreting the overall emission (see Section 6). The data are shown in Figs 5 and 6.

5.1 Radio observations

We collected radio observations from Rhodes et al. (2022). These late-time observations have been performed with e-MERLIN, the VLA, and MeerKAT, and cover the $\sim$1 – 10 GHz frequency range. There are no simultaneous detections available at higher frequencies at the time of radio detections, which span the temporal window $\sim$5 – 56 d after T_0. Rhodes et al. (2022) argue that the emission detected in the radio band is dominated by a different component as compared to the emission detected at earlier times in the optical band and in X-rays, and they suggest radiation from the cocoon as possible explanation. In our analysis we also find that radio data cannot be easily explained as synchrotron radiation from the forward shock driven by the relativistic jet, see the discussion in Section 6. We nevertheless include radio data in our analysis (star symbols in Figs 5 and 6), verifying that the estimation of the synchrotron flux from the jet given by the modelling lies below the observed radio emission.

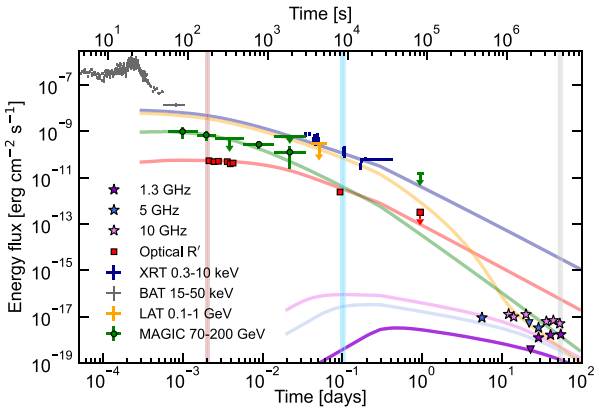

Figure 5. Multiwavelength light curves of GRB 201216C. Both the X-ray and optical observations have been corrected accounting for absorption. MAGIC data points are EBL-corrected. Upside down triangles represent upper limits. Solid curves show the best fit model obtained in a synchrotron – SSC forward shock scenario. Different colours refer to the different wavelengths where observations are available (see the legend). The modelling is obtained with the following parameters: $E_{\rm k} = 4 \times 10^{53}$ erg, $\epsilon_{\rm e} = 0.08$, $\epsilon_{\rm B} = 2.5 \times 10^{-3}$, $A_\star = 2.5 \times 10^{-2}$, $p = 2.1$, $\Gamma_0 = 180$, and $\theta_{\rm jet} = 1^\circ$. Vertical lines mark the times where SED have been built (see Fig. 6).

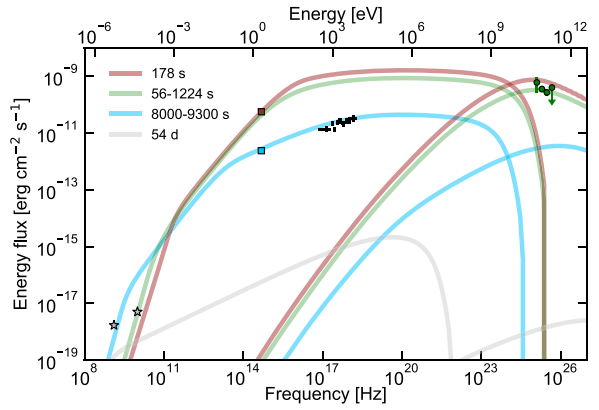

Figure 6. SEDs of GRB 201216C at different times. Different colours for curves and data points refer to different times (see the legend). The times where the SEDs are calculated are also marked in Fig. 5 with vertical stripes. Solid curves show the synchrotron and SSC theoretical spectra for the same parameters used for Fig. 5. De-absorbed optical data in the r' filter are marked with square symbols, while star symbols are observations at 1.3 and 10 GHz at 54.5 and 53 d, respectively (from Rhodes et al. 2022). The XRT spectral data points estimated around 9000 s are also shown. Green circles show the MAGIC spectrum averaged between 56 and 1224 s (Fig. 3). The theoretical SED to be compared with the MAGIC spectrum is the green curve, which shows the predicted spectrum (synchrotron + SSC) averaged in the same time window (56–1224 s).

5.2 Optical observations: the LT and VLT

The 2-m fully robotic LT autonomously reacted (Guidorzi et al. 2006) to the *Swift*-BAT alert, and started observations from about 178 s after the burst with the IO:O[5] optical camera in the SDSS-r band (Shrestha et al. 2020). The light curve of GRB 201216C optical counterpart initially displayed a flat behaviour (see Fig. 5) followed by a steepening, as revealed by VLT data gathered at 2.2 h post-burst (Izzo, Malesani & Kann 2020) and by the non-detection of the afterglow in deeper LT observations at 1 d post-burst. We note that the LT photometry data were calibrated using a common set of stars present in the field of view selected from the APASS catalogue.

5.3 X-ray observations

Swift-XRT started to collect data on GRB 201216C only 2966.8 s after the burst onset due to an observing constraint (Beardmore et al. 2020). Observations continued up to $T_0 + 4325.4$ s. The unabsorbed X-ray flux integrated in the 0.3–10 keV energy range is shown in Fig. 5 (blue data points).

At around 0.1 d XRT and optical data are simultaneously available and we built the spectral energy distribution (SED) around this time (Fig. 6). The XRT spectrum has been derived by analysing data between 8900 and 9300 s with the XSPEC software. Source and background spectra have been built using the automatic analysis tool[6] We modelled the spectrum with an absorbed power-law accounting both for Galactic and intrinsic metal absorption using the xspec models *tbabs* and *ztbabs*, respectively. The Galactic contribution is fixed to the value $N_{\rm H,\,G} = 5.04 \times 10^{20}$ cm^{-2} (Willingale et al. 2013), while the column density in the host galaxy is a free parameter. We find that the best fit photon index is -1.67 ± 0.19 and the intrinsic column density is $N_{\rm H} = (1.48 \pm 0.52) \times 10^{22}$ cm^{-2}. The spectral data, rebinned for plotting purposes and de-absorbed for both Galactic and intrinsic absorption, are shown in Fig. 6 (black crosses).

5.4 Gamma-ray observations by *Fermi*-LAT

Fermi-LAT observations started from $T_0 + 3500$ s and continued until the GRB position was no longer visible ($T_0 + 5500$ s). No signal is detected during this time window. Assuming a photon index $\alpha = -2$, the estimated upper limit in the energy range 0.1–1 GeV is 3×10^{-10} erg/ cm^2 s^{-1} (Bissaldi et al. 2020). This upper limit is included in our analysis (orange arrow in Fig. 5).

All the light curves at different frequencies are shown in Fig. 5. The *Swift*-BAT prompt emission light curve is also included in the figure (grey data points). The BAT flux is integrated in the 15–50 keV energy range and points are rebinned using a signal-to-noise ratio (SNR) criterion equal to seven.[7] The vertical coloured stripes mark the times where SEDs are built. The SEDs are shown in Fig. 6, where the MAGIC spectrum integrated between 56 and 1224 s is also shown.

6 MODELLING

In this Section, we discuss the origin of the emission detected by MAGIC and its connection to the afterglow emission at lower energies, from radio to X-rays. In particular, we test an SSC scenario from electrons accelerated at the forward shock. We consider a relativistic jet with initial Lorentz factor $\Gamma_0 \gg 1$, opening angle $\theta_{\rm jet}$, and a top-hat geometry. The (isotropic equivalent) kinetic energy of the jet $E_{\rm k}$ is related to $E_{\rm iso,\,\gamma} \sim 6 \times 10^{53}$ erg (see Section 2) through the efficiency for production of prompt radiation η_γ: $E_{\rm k} = \frac{1-\eta_\gamma}{\eta_\gamma} E_{\rm iso,\gamma}$. The details of the equations adopted to describe the dynamics, the particle acceleration, and the radiative output can be found in Miceli & Nava (2022) and are also reported in Appendix A. We summarize here the general model and the main assumptions.

[5] https://telescope.livjm.ac.uk/TelInst/Inst/IOO/

[6] https://www.swift.ac.uk/xrt_spectra/01013243/

[7] https://www.swift.ac.uk/burst_analyser/01013243/

The jet is expanding in an ambient medium characterized by a density described by a power-law function $n(R) \propto R^{-s}$. We consider the density to be either constant ($s = 0$ and $n(R) = n_0$) or shaped by the progenitor stellar wind: $n(R) = AR^{-2}$ ($s = 2$), where A is related to the mass-loss rate of the progenitor's star $\dot{M}$ and to the velocity of the wind v_w by $A = \dot{M}/4\pi\, m_p\, v_w$ (m_p is the mass of the proton). We normalize the value of A to a mass-loss rate of 10^{-5} solar masses per year and a wind velocity of 10^3 km s^{-1}: $A = 3 \times 10^{35}\, A_\star$ cm^{-1}. We assume that ambient electrons are accelerated at the forward shock into a power-law distribution $dN/d\gamma \propto \gamma^{-p}$ from γ_{min} and γ_{max}. The bulk Lorentz factor of the fluid just behind the shock is assumed to be constant ($\Gamma = \Gamma_0$) before the deceleration and described by the solution given by Blandford & McKee (1976) ($\Gamma = \Gamma_{BM}$) during the deceleration (note that the equation given by Blandford & McKee (1976) describes the Lorentz factor of the shock Γ_{sh}, which we relate to the Lorentz factor of the fluid using $\Gamma = \Gamma_{sh}/\sqrt{2}$). The two regimes are smoothly connected to obtain the description of the bulk Lorentz factor of the fluid just behind the shock as a function of shock radius.

To infer the particle distribution and the photon spectrum at any time t we numerically evolve the equations describing the electron and photon populations including adiabatic losses, synchrotron emission and self-absorption, inverse Compton emission and $\gamma - \gamma$ annihilation, and pair production. To relate the comoving properties computed by the code to the observed one, we assume that the emission received at a given observer time is dominated by electrons moving at an angle $\cos\theta = \beta$ from the line of sight to the observer, where β is the velocity of the shocked fluid.

Before presenting the results of the numerical modelling, we discuss some general considerations that can be inferred using analytic approximations from Granot & Sari (2002). Fig. 5 shows that the optical flux is nearly constant up to at least 5×10^{-3} d. At later times this behaviour breaks into a steeper temporal decay. We take as reference value for the break time $\sim 10^{-2}$ d. This behaviour of the optical light curve can be explained if the break frequency ν_m (i.e. the typical photon energy emitted by electrons with Lorentz factor γ_{min}) is crossing the r band. The nearly constant flux before the crossing time is indicative of a wind-shaped external medium (i.e. s = 2). The preference for a wind-like medium is also supported by the lack of a phase of increasing flux in the MAGIC observations, which start as early as ∼60 s after the onset of the prompt emission. Since $\nu_m \propto t^{-1.5}$, we expect $\nu_m \sim 1$ GHz at ∼50 d. Observations at 1.3 GHz do not allow to constrain the peak time, but we notice that they are consistent with the presence of a peak around 50 d (a zoom on radio observations can be found in fig. 1 of Rhodes et al. 2022 and it shows that, considering the errors, the flux is consistent with being constant at about 50 d). The radio SED at this time (see Fig. 6 and also Rhodes et al. 2022) shows that the self-absorption frequency ν_{sa} must be below 1 GHz. Since $\nu_{sa} \propto t^{-3/5}$, this implies that during the time spanned by observations $\nu_{sa} < \nu_m$. The fast increase of the 1.3 GHz flux (with temporal index $\gtrsim 5$, as reported in Rhodes et al. 2022) however implies that observations at this time are below the self-absorption frequency (otherwise the flux at 1.3 GHz should be constant), constraining $\nu_{sa}(50\,\mathrm{d}) \sim 1$ GHz.

To summarize, the scenario implied by optical and radio observations invokes a jet expanding in a wind-like density and producing a synchrotron spectrum with $\nu_{sa} < \nu_m$, and ν_m crossing the optical r band at $\sim 10^{-2}$ d and the 1 GHz frequency at ∼50 d. We now check the consistency of this interpretation with X-ray observations. Imposing $\nu_m(54\,\mathrm{d}) = \nu_{sa}(54\,\mathrm{d}) = 1$ GHz and the flux $F(\nu_{sa}, 54\,\mathrm{d}) = 2 \times 10^{-18}$ erg cm^{-2} s^{-1}, and using equations for the break frequencies and flux in a wind-like medium from Granot & Sari (2002), it is possible to derive the values of E_k, ϵ_B, and $A_\star$ as a function of ϵ_e, for fixed values of p. For $p = 2.2$ we find $E_{k,52} \simeq \epsilon_e$, $\epsilon_B \simeq 2.3 \times 10^{-6}\epsilon_e^{-5}$, and $A_\star \simeq 8.8\,\epsilon_e^2$. This shows that the requirement that the F_ν spectrum peaks at $\nu_{sa} = 1$ GHz at 54 d limits the energy to a low value $E_k < 10^{52}$ erg, inconsistent with the large flux detected in the X-ray afterglow. In particular we find that the X-ray band is always above the cooling frequency ν_c for different assumptions on ϵ_e. Moreover, in this range, the predicted flux is at least one order of magnitude below the detected X-ray flux. This statement is quite robust, as the flux in this band weakly depends on ϵ_B, does not depend on $A_\star$, and is proportional to $E_k\,\epsilon_e$. Pushing ϵ_e to large values (close to one) improves the situation, at the expense of a very small ϵ_B, implying a large SSC component. This solution is ruled out by MAGIC observations.

Table 2. List of the input parameters for the afterglow model. For each parameter, the range of values investigated by means of the numerical model are listed in the second column. Solutions are not found for an homogeneous density medium (s = 0). The last column list the values that better fit the observations and used to produce the model light curves and model SEDs in Figs 5 and 6.

Parameter	Range	Best fit value
E_k [erg]	$10^{50} - 10^{54}$	4×10^{53}
θ_{jet} [degrees]	0.5 – 3	1
Γ_0	80–300	180
n_0 [cm^{-3}] ($s = 0$)	$10^{-2} - 10^{2}$	-
$A_\star$ ($s = 2$)	$10^{-2} - 10^{2}$	2.5×10^{-2}
p	2.05–2.6	2.1
ϵ_e	0.01–0.9	0.08
ϵ_B	$10^{-7} - 10^{-1}$	2.5×10^{-3}

Being unable to find a scenario that explains all the available data as synchrotron and SSC emission from the forward shock driven by a relativistic jet, we consider the possibility that late-time radio emission is dominated by a different component, as also concluded by Rhodes et al. (2022), which identify in a wider mildly (or non-) relativistic cocoon the origin of the radio emission. We then restrict the modelling to the MAGIC, X-ray and optical data, requiring that the flux at 1–10 GHz from the narrow relativistic jet is below the observed flux.

We performed numerical calculations of the expected synchrotron and SSC radiation and their evolution in time for wide ranges of values of the parameters E_k, ϵ_e, ϵ_B, p, $n(R)$, θ_{jet}, and Γ_0. The investigated range of values for each parameter is reported in Table 2. The numerical calculations confirm the considerations derived from analytic estimates. In particular, we neither find a solution for a homogeneous medium nor for a complete description of radio to GeV observations. Assuming a wind-like density profile, we find that the observations can be well described as synchrotron and SSC radiation. In particular, once the request to model also radio observations with forward shock emission from the relativistic jet is abandoned, the X-ray flux can be explained by increasing the assumed value of the jet energy, which also moves the self-absorption frequency to lower energies. An example of modelling is provided in Figs 5 and 6, where observations (corrected for absorption in the optical and X-ray band) are compared to the light curves and spectra predicted with the following parameters: $E_k = 4 \times 10^{53}$ erg, $\epsilon_e = 0.08$, $\epsilon_B = 2.5 \times 10^{-3}$, $A_\star = 2.5 \times 10^{-2}$, $p = 2.1$, $\Gamma_0 = 180$, and $\theta_{jet} = 1^\circ$ the values are listed also in Table 2. The jet opening angle is broadly constrained by the need to not overproduce the radio flux. The inferred value points to a narrow jet, with opening angle in the low-value tail of distributions of inferred jet opening angles for long GRBs (Chen et al. 2020). We note that a similarly small ($\theta_{jet} \sim 0.8^\circ$) value for the jet opening angle has

been inferred for the TeV GRB 221009A LHAASO Collaboration et al. (2023). The inferred jet kinetic energy implies an efficiency of the prompt emission $\eta_\gamma \simeq 60$ per cent. In agreement with the steep optical spectrum reported by Vielfaure et al. (2020), this model implies an extinction of 4.6 magnitudes in the r' band, which is well in excess of the Galactic contribution ($E(B-V) = 0.05$). As it can be seen from Fig. 5, the onset of the deceleration occurs at $t_{\rm obs} \lesssim 200$ s, where the X-ray and TeV theoretical light curves steepen from an almost flat to a decaying flux.

The steepening of the optical light curve instead occurs at $\sim 10^3$ s because, as already commented, it is determined by the $\nu_{\rm m}$ frequency crossing the r band. In this interpretation, the frequency $\nu_{\rm m}$ is initially above the optical band (see the brown SED in Fig. 6) and then moves to lower frequencies crossing the optical and explaining the steepening in the light curve. X-ray observations lie just above the cooling frequency, but the X-ray spectrum remains harder than expected due to the role of the Klein–Nishina cross-section. We also computed the expected SED averaged between 56 and 1224 s, where the MAGIC spectrum (see Fig. 3) is computed. The model SED is reported in Fig. 6 (green curve, to be compared with the MAGIC data, green circles). We find that the $\gamma - \gamma$ internal absorption plays a minor role in shaping the spectrum: the flux reduction at 200 GeV is about 25 per cent. In the same figure it is also possible to see the expected location of the maximum energy of synchrotron photons, initially located at 10 GeV at the time of the first SED, and then moving towards lower energies. Assuming diffusive shock acceleration proceeding at the maximum rate rules out a synchrotron origin for the photons detected by MAGIC.

7 CONCLUSIONS

In this paper, MAGIC analysis results on GRB 201216C and their interpretation were presented. The GRB afterglow was observed at early times ($\sim 10^2 - 10^3$ s) by MAGIC for a total of $\sim$2.5 h during the first night and detected at the level of 6σ in the first 20 min. This is the second firm detection of a GRB with the MAGIC telescopes after GRB 190114C, and also the farthest VHE source detected to date. Both the observed and intrinsic average spectra can be well described by a power-law. A time-resolved analysis was also performed, in order to evaluate the temporal behaviour of VHE emission. The obtained light curve shows a monotonic power-law decay, indicating a probable afterglow origin of the VHE emission.

Multiwavelength data were also collected by other ground- and space-based instruments. Unfortunately, most of them are not contemporaneous to the first MAGIC observation time window. In other cases, as for *Fermi*-LAT, the GRB could not be detected. Like other GRBs detected in the VHE range, multiwavelength data were used to perform a modelling of the broad-band emission. In this manuscript a synchrotron and SSC radiation model at the forward shock in the afterglow was considered. SEDs built at different times show that synchrotron photons can reach a maximum energy of 10 GeV about three minutes after the GRB onset. The emission detected by MAGIC reaches higher energies, and can therefore be explained by the SSC component of the model. By comparing analytic estimates and the numerical modelling, evidence for the need of a different component at the origin of late-time radio emission is found, in agreement with previously published studies on this GRB. Both observations and modelling support a wind-like medium, as expected in the case of a long GRB. The best fit model parameters are found to be consistent with those estimated in previous studies of GRB afterglows without VHE detection. This proves the flexibility of the SSC scenario in describing the VHE emission of GRBs.

Like other VHE detected GRBs (GRB 180720B and GRB 190114C), 201216C was a bright GRB, allowing for a detection in spite of the high redshift. Once again, the rapid response and low-energy threshold of the MAGIC telescopes to GRB alerts was crucial to detect the VHE emission in the early afterglow phase. Altogether, the detection by MAGIC and other experiments of several bursts so far suggests that VHE emission is common both in high- and low-luminosity GRBs. Other VHE detected GRBs showed a correlation between the intrinsic emission in the X-ray and VHE bands, where a similar time decay and flux value were observed. In the case of GRB 201216C such a direct comparison cannot be performed given the lack of contemporaneous data in the two bands. The extrapolation of the X-ray flux into the first MAGIC time window, assuming a smooth power-law behaviour typical of the afterglow phase, shows that the VHE flux is lower than the X-ray one. However, one should take into account the rather narrow energy range of the VHE detection due to the large absorption caused by the EBL.

ACKNOWLEDGEMENTS

The MAGIC collaboration would like to thank the Instituto de Astrofísica de Canarias for the excellent working conditions at the Observatorio del Roque de los Muchachos in La Palma. The financial support of the German BMBF, MPG, and HGF; the Italian INFN and INAF; the Swiss National Fund SNF; the grants PID2019-104114RB-C31, PID2019-104114RB-C32, PID2019-104114RB-C33, PID2019-105510GB-C31, PID2019-107847RB-C41, PID2019-107847RB-C42, PID2019-107847RB-C44, PID2019-107988GB-C22, PID2020-118491GB-I00 funded by the Spanish MCIN/AEI/ 10.13039/501100011033; the Indian Department of Atomic Energy; the Japanese ICRR, the University of Tokyo, JSPS, and MEXT; the Bulgarian Ministry of Education and Science, National RI Roadmap Project DO1-400/18.12.2020 and the Academy of Finland grant number 320045 is gratefully acknowledged. This work was also been supported by Centros de Excelencia 'Severo Ochoa' y Unidades 'María de Maeztu' programme of the Spanish MCIN/AEI/ 10.13039/501100011033 (SEV-2016-0588, CEX2019-000920-S, CEX2019-000918-M, CEX2021-001131-S, MDM-2015-0509-18-2) and by the CERCA institution of the Generalitat de Catalunya; by the Croatian Science Foundation (HrZZ) Project IP-2016-06-9782 and the University of Rijeka Project uniri-prirod-18-48; by the Deutsche Forschungsgemeinschaft (SFB1491 and SFB876); the Polish Ministry Of Education and Science grant number 2021/WK/08; and by the Brazilian MCTIC, CNPq, and FAPERJ. This work was supported by JSPS KAKENHI grant number JP21K20368. LN acknowledges partial support from the INAF Mini-grant 'Shock acceleration in Gamma Ray Bursts'.

The LT is operated on the island of La Palma by Liverpool John Moores University in the Spanish Observatorio del Roque de los Muchachos of the Instituto de Astrofisica de Canarias with financial support from the UK Science and Technology Facilities Council (STFC) under UKRI grant number ST/T00147X/1. MS and IS thank UKRI/STFC for financial support (grant no. ST/R000484/1).

We would like to thank the STARGATE collaboration for the confirmation of the redshift of the source via private communication.

DATA AVAILABILITY

The data underlying this article will be shared on reasonable request to the corresponding authors.

REFERENCES

Abbott B. P. et al., 2017, Phys. Rev. Lett., 119, 161101
Abdalla H. et al., 2019, Nature, 575, 464
Acciari V. A. et al., 2021, ApJ, 908, L90
Ackermann M. et al., 2014, Science, 343, 42
Albert J. et al., 2007, Nucl. Instrum. Methods. Phys. Res. A, 583, 494
Aleksić J. et al., 2016, ApJ, 72, L76
Amati L. et al., 2002, A&A, 390, 81
Ayala H., 2020, GRB Coordinates Network, 29086, 1
Beardmore A. P. et al., 2020, GRB Coordinates Network, 29061, 1
Bissaldi E., Omodei N., Kocevski D., Axelsson M., Longo F., Moretti E., Fermi-LAT Collaboration, 2020, GRB Coordinates Network, 29076, 1
Blandford R. D., McKee C. F., 1976, Phys. Fluids, 19, 1130
Chang J. S., Cooper G., 1970, J. Comput. Phys., 6, 1
Chen W. J., Urata Y., Huang K., Takahashi S., Petitpas G., Asada K., 2020, ApJL, 891, L15
Dazzi F. et al., 2021, IEEE Transactions on Nuclear Science, 68, 1473
de Jager O. C., Harding A. K., Michelson P. F., Nel H. I., Nolan P. L., Sreekumar P., Thompson D. J., 1996, ApJ, 457, L253
Derishev E., Piran T., 2021, ApJ, 923, L135
Domínguez A. et al., 2011, MNRAS, 410, 2556 (D11)
Finke J. D., Razzaque S., Dermer C. D., 2010, ApJ, 712, L238 (F08)
Franceschini A., Rodighiero G., Vaccari M., 2008, A&A, 487, 837
Fruck C. et al., 2022, MNRAS, 515, 4520
Ghisellini G., Guilbert P. W., Svensson R., 1988, ApJ, 334, L5
Gilmore R. C., Somerville R. S., Primack J. R., Domínguez A., 2012, MNRAS, 422, 3189
Goldstein A. et al., 2017, ApJ, 848, L14
Granot J., Sari R., 2002, ApJ, 568, L820
Guidorzi C. et al., 2006, PASP, 118, 288
H. E. S. S. Collaboration et al., 2021, Science, 372, 1081
Izzo L., Malesani D. B., Kann D. A., 2020, GRB Coordinates Network, 29066, 1
Jones F. C., 1968, Phys. Rev., 167, 1159
Kumar P., Zhang B., 2015, Phys. Rep., 561, 1
Kumar P., Hernández R. A., Bošnjak Ž., Barniol Duran R., 2012, MNRAS, 427
LHAASO Collaboration et al., 2023, Science, 380, 1390
Li T. P., Ma Y. Q., 1983, ApJ, 272, L317
MAGIC Collaboration et al., 2019a, Nature, 575, 455
MAGIC Collaboration et al., 2019b, Nature, 575, 459
MAGIC Collaboration et al., 2020, A&A, 643, 14
Malacaria C., Veres P., Meegan C., Bissaldi E., Fermi GBM Team, 2020, GRB Coordinates Network, 29073, 1
Mészáros P., 2002, ARA&A, 40, 137
Miceli D., Nava L., 2022, Galaxies, 10, 66
Mirzoyan R. et al., 2019, GRB Coordinates Network, 23701, 1
Nava L., Sironi L., Ghisellini G., Celotti A., Ghirlanda G., 2013, MNRAS, 433, 2107
Oganesyan G., Nava L., Ghirlanda G., Celotti A., 2017, ApJ, 846, L137
Oganesyan G., Nava L., Ghirlanda G., Celotti A., 2018, A&A, 616, 138
Oganesyan G., Nava L., Ghirlanda G., Melandri A., Celotti A., 2019, A&A, 628, 59
Panaitescu A., Kumar P., 2000, ApJ, 543, L66
Pennanen T., Vurm I., Poutanen J., 2014, A&A, 564, 77
Piran T., 2004, Rev. Mod. Phys., 76, 1143
Piran T., Nakar E., 2010, ApJL, 718, L63
Piron F. et al., 2001, A&A, 374, 895
Rhodes L., van der Horst A. J., Fender R., Aguilera-Dena D. R., Bright J. S., Vergani S., Williams D. R. A., 2022, MNRAS, 513, 1895
Rolke W. A., López A. M., 2001, Nuclear Instruments and Methods in Physics Research A, 458, 745
Rybicki G. B., Lightman A. P., 1979, A Wiley-Interscience Publication. Wiley, New York
Sari R., Piran T., Narayan R., 1998, ApJL, 497, L17
Schmuckermaier F. et al., 2023, A&A, 673, 2
Shayduk M., 2013, In Proceedings of the 33rd International Cosmic Ray Conference (ICRC2013). Rio de Janeiro, Brazil
Shrestha M., Melandri A., Smith R., Steele I. A., Kobayashi S., Mundell C., Gomboc A., Guidorzi C., 2020, GRB Coordinates Network, 29085, 1
Ukwatta T. N. et al., 2020, GRB Coordinates Network, 29080, 1
Vielfaure J. B. et al., 2020, GRB Coordinates Network, 29077, 1
Wang X.-Y., Liu R.-Y., Zhang H.-M., Xi S.-Q., Zhang B., 2019, ApJ, 884, L117
Willingale R., Starling R. L. C., Beardmore A. P., Tanvir N. R., O'Brien P. T., 2013, MNRAS, 431, 394
Woosley S. E., Bloom J. S., 2006, ARA&A, 44, 507
Yonetoku D., Murakami T., Nakamura T., Yamazaki R., Inoue A. K., Ioka K., 2004, ApJ, 609, L935
Zanin R. et al., 2013, in International Cosmic Ray Conference. p. 2937
Zhang B.-B., Uhm Z. L., Connaughton V., Briggs M. S., Zhang B., 2016, ApJ, 816, L72
Zhang L.-L., Ren J., Wang Y., Liang E.-W., 2023, ApJ, 952, L127
Zhao X., Li Z., Liu X., Zhang B.-b., Bai J., Mészáros P., 2014, ApJ, 780, L12

APPENDIX: NUMERICAL AFTERGLOW MODEL

In this section, we summarize the equations adopted to describe the synchrotron and SSC emission from electrons accelerated in the forward shock driven by a relativistic jet ($\Gamma \gg 1$) in the surrounding medium. The list of the free model parameters can be found in Table 2. More details can be found in Miceli & Nava (2022).

Circumburst medium

The surrounding medium is assumed to have a radial density profile $n(R)$ described by a power-law function: $n(R) = AR^{-s}$, where R is the distance of the shock front from the center of the explosion and n is the number density. Two possibilities are investigated: $s = 0$ ($n(R) =$ constant) and $s = 2$ ($n(R) = A\,R^{-2}$). In the latter case, the normalization A is related to the mass-loss rate of the progenitor's star $\dot{M}$ and to the velocity of the wind $v_{\rm w}$ by $A = \dot{M}/4\,\pi\,m_{\rm p}\,v_{\rm w}$ ($m_{\rm p}$ is the proton mass). We normalize the value of A to a mass-loss rate of 10^{-5} solar masses per year and a wind velocity of 10^3 km s^{-1}: $A = 3 \times 10^{35} A_\star$ cm^{-1}.

Blast-wave dynamics

The evolution of the Lorentz factor of a decelerating relativistic adiabatic blastwave has been derived by Blandford & McKee (1976) (BM), which provides the shock Lorentz factor, its relation with the Lorentz factor of the shocked fluid just behind the shock, and the profile of the Lorentz factor in the downstream region. We consider the BM solution to describe the Lorentz factor of the shock $\Gamma_{\rm sh}$:

$$\Gamma_{\rm sh,BM}(R) = \left[\frac{(17-4s)\,E_{\rm k}}{8\pi\,A\,m_{\rm p}c^2\,R^{(3-s)}}\right]^{1/2}, \tag{A1}$$

where the Lorentz factor of the fluid just behind the shock (Γ) is given by:

$$\Gamma = \frac{\Gamma_{\rm sh}}{\sqrt{2}}. \tag{A2}$$

We do not take into account its profile in the downstream region (homogeneous shell approximation).

The BM solution is valid only during the deceleration, in particular when the energy of the ejecta is negligible compared to the energy transferred to the shocked external medium. Well before the deceleration begins, the Lorentz factor is constant and equal to its initial

value Γ_0. To describe the entire evolution, we smoothly connect the initial phase to the deceleration phase:

$$\Gamma = \Gamma_0 \left[1 + \left(\frac{\Gamma_0}{\Gamma_{\rm BM}}\right)^q\right]^{-1/q}. \quad \text{(A3)}$$

For fitting purposes, in GRB 201216C the smoothing factor q has been kept fixed to the value $q = 3$ to describe the transition from the coasting to the deceleration phase.

Particle acceleration and magnetic field acceleration

The accelerated electrons are assumed to have a spectrum described by a power-law: $dN^{\rm acc}(\gamma)/d\gamma \propto \gamma^{-p}$ for $\gamma_{\rm min} \leq \gamma \leq \gamma_{\rm max}$, where $\gamma_{\rm min}$ and $\gamma_{\rm max}$ are the minimum and maximum Lorentz factors at which electrons are accelerated.

The value of $\gamma_{\rm max}$ is obtained by imposing that the synchrotron cooling time is equal to the acceleration time, set by the assumption that the particles mean free path is equal to their Larmor radius. This leads to

$$\gamma_{\rm max} = \sqrt{\frac{6\pi\, q}{\sigma_{\rm T} B}}. \quad \text{(A4)}$$

For a discussion on the maximum energy, see also (Kumar et al. 2012; Derishev & Piran 2021), which use the same or similar equations, differing at most by a numerical factor of the order of unity.

Since a fraction ϵ_e of the shock-dissipated energy goes into the acceleration of electrons into a non-thermal distribution, their average random Lorentz factor $\langle\gamma\rangle$ is

$$\langle\gamma\rangle = \epsilon_{\rm e}\frac{m_{\rm p}}{m_{\rm e}}(\Gamma - 1), \quad \text{(A5)}$$

the minimum Lorentz factor is found after numerically solving the equation

$$\left[\frac{\gamma_{\rm min}^{-p+2} - \gamma_{\rm max}^{-p+2}}{\gamma_{\rm min}^{-p+1} - \gamma_{\rm max}^{-p+1}}\right] = \epsilon_e \frac{m_{\rm p}}{m_{\rm e}}\frac{p-2}{p-1}(\Gamma - 1) \qquad \text{if } p \neq 2. \quad \text{(A6)}$$

For $\gamma_{\rm max}^{-p+2} \ll \gamma_{\rm min}^{-p+2}$, the equation reduces to the widely used one:

$$\gamma_{\rm min} = \epsilon_{\rm e}\frac{m_{\rm p}}{m_{\rm e}}\frac{p-2}{p-1}(\Gamma - 1). \quad \text{(A7)}$$

Because we find that the best fit of GRB 201216C requires $p \sim 2.1$, we use the full equation for the estimate of $\gamma_{\rm min}$. Using the approximated one would result in underestimating $\gamma_{\rm min}$ and in the non-conservation of the number and total energy of the accelerated electrons.

A fraction ϵ_B of the shock-dissipated energy is used to amplify the magnetic field, giving

$$B = \sqrt{32\pi\, \epsilon_B m_{\rm p} c^2\, n(r)}\,\Gamma \quad \text{(A8)}$$

The evolution of the electron distribution

The temporal evolution of the particle distribution $N(\gamma, t')$ as a function of the electron Lorentz factor γ and the comoving time t' is described by the differential equation

$$\frac{\partial N(\gamma, t')}{\partial t'} = \frac{\partial}{\partial \gamma}\left[\dot{\gamma} N(\gamma, t')\right] + Q(\gamma), \quad \text{(A9)}$$

where $\dot{\gamma} = \partial\gamma/\partial t'$ is the rate of change of the Lorentz factor γ of an electron caused by adiabatic, synchrotron, and SSC losses and by energy gains due to absorption of synchrotron photons (synchrotron self-absorption, SSA).

The source term $Q(\gamma, t') = Q^{\rm acc}(\gamma, t') + Q^{\rm pp}(\gamma, t')$ describes the injection of freshly accelerated particles ($Q^{\rm acc}(\gamma, t') = dN^{\rm acc}/d\gamma\, dt'$) and the injection of pairs $Q^{\rm pp}(\gamma, t')$ produced by photon–photon annihilation.

To solve the equation, we adopt an implicit finite difference scheme based on the discretization method proposed by Chang & Cooper (1970).

Electron energy losses

The synchrotron power emitted by an electron with Lorentz factor γ depends on the pitch angle, that is, the angle between the electron velocity and the magnetic field line. We assume that the electrons have an isotropic pitch angle distribution and use equations that are averaged over the pitch angle. The synchrotron cooling rate of an electron with Lorentz factor γ is given by

$$\dot{\gamma}_{\rm syn} \equiv \left.\frac{d\gamma}{dt'}\right|_{\rm syn} = -\frac{\sigma_T \gamma^2 B'^2}{6\pi\, m_e c}. \quad \text{(A10)}$$

The energy loss term for the SSC is calculated with the equation

$$\dot{\gamma}_{\rm SSC} = \left.\frac{d\gamma}{dt'}\right|_{\rm SSC} = -\frac{3h\sigma_t}{4m_e c\gamma^2}\int d\nu' \nu' \int \frac{d\tilde{\nu}'}{\tilde{\nu}'} n_{\tilde{\nu}'}(t') K(\gamma, \nu', \tilde{\nu}'), \quad \text{(A11)}$$

where $\tilde{\nu}'$ and ν' are the frequencies (in the comoving frame) of the photon before and after the scattering, respectively. For the expression of $K(\gamma, \nu', \tilde{\nu}')$ we adopt the formulation proposed in Jones (1968), which is valid both in Thomson and Klein–Nishina regime, and describes both the down-scattering (i.e. $\nu' < \tilde{\nu}'$) and the up-scattering (i.e. $\nu' > \tilde{\nu}'$) process.

Particles loose their energy also adiabatically, due to the spreading of the emission region:

$$\dot{\gamma}_{\rm ad} = \left.\frac{d\gamma}{dt'}\right|_{\rm ad} = -\frac{\gamma\beta^2}{3}\frac{d\ln V'}{dt'}. \quad \text{(A12)}$$

The comoving volume V' of the emission region can be estimated considering that the contact discontinuity is moving away from the shock at a velocity $c/3$ (Pennanen, Vurm & Poutanen 2014). After a time $t' = \int dR/\Gamma(R)\, c$ the comoving volume is

$$V' = 4\pi R^2 \frac{ct'}{3}, \quad \text{(A13)}$$

Estimate of the radiative output

Following Ghisellini, Guilbert & Svensson (1988), the synchrotron spectrum emitted by an electron with Lorentz factor γ, averaged over an isotropic pitch angle distribution is

$$P'^{\rm syn}_{\nu'}(\nu', \gamma) = \frac{2\sqrt{3}\, e^3\, B'}{m_{\rm e}\, c^2}\, x^2 \times \\ \times \left[K_{4/3}(x)\, K_{1/3}(x) - 0.6x(K^2_{4/3}(x) - K^2_{1/3}(x))\right], \quad \text{(A14)}$$

where $x \equiv \nu'\, 4\pi\, m_{\rm e} c/(6\, q\, B'\gamma^2)$, and $K_{\rm n}$ are the modified Bessel functions of order n. The total power emitted at the frequency ν' is obtained integrating over the electron distribution:

$$P'^{\rm syn}_{\nu'}(\nu') = \int P'^{\rm syn}_{\nu'}(\nu', \gamma)\frac{dN}{d\gamma} d\gamma. \quad \text{(A15)}$$

The SSC radiation emitted by an electron with Lorentz factor γ can be calculated as

$$P^{\rm SSC}_{\nu'}(\nu', \gamma) = \frac{3}{4} h\sigma_{\rm T} c \frac{\nu'}{\gamma^2} \int \frac{d\tilde{\nu}'}{\tilde{\nu}'} n_{\tilde{\nu}'} K(\gamma, \nu', \tilde{\nu}'), \tag{A16}$$

where $n_{\tilde{\nu}'}$ is the photon density of synchrotron photons and the integration is performed over the entire synchrotron spectrum. Integration over the electron distribution provides the total SSC emitted power at frequency ν'.

Absorption processes

Electrons can re-absorb low-energy photons before they escape from the source region. The cross-section of the process is (Rybicki & Lightman 1979):

$$\sigma(\nu', \gamma) = -\frac{1}{8\pi \nu'^2 m_{\rm e}} \frac{P'(\gamma, \nu')\gamma^2}{N(\gamma)} \frac{\partial}{\partial \gamma} \left[\frac{N(\gamma)}{\gamma^2}\right] \tag{A17}$$

valid for any radiation mechanism at the emission frequency ν', with $P'(\gamma, \nu')$ being the specific power of electrons with Lorentz factor γ at frequency ν' and assuming $h\nu' \ll \gamma m_{\rm e} c^2$.

While the SSA mechanism will affect mostly the low-frequency range, at the highest energies the flux can be attenuated by photon–photon annihilation. For the cross-section $\sigma(\nu' \nu'_t)$ (where $n'(\nu'_t)$ is the number density of the target photons) we use the equation

$$\sigma(\nu', \nu'_t) = \frac{3}{16}\sigma_T(1-\beta'^2)\left[(3-\beta'^4)\ln\left(\frac{1+\beta'}{1-\beta'}\right) - 2\beta'(2-\beta'^2)\right], \tag{A18}$$

where

$$\beta'(\omega_t, \omega_s, \mu) = \left[1 - \frac{2}{\omega_t \omega_s (1-\mu)}\right]^{\frac{1}{2}} \tag{A19}$$

and $\omega_t = h\nu'_t/m_e c^2$ with ν'_t being the target photon frequency, $\omega_s = h\nu'/m_e c^2$ with ν' being the source photon frequency and $\mu = \cos\phi$, where ϕ is the scattering angle. Then, it is possible to derive the annihilation rate of photons into electron–positron pairs as

$$R(\omega_t, \omega_s) = c \int_{-1}^{\mu_{max}} \frac{d\mu}{2}(1-\mu)\sigma_{\gamma\gamma}(\omega_t, \omega_s, \mu), \tag{A20}$$

where $\mu_{max} = \max(-1, 1 - 2/\omega_s\omega_t)$ coming from the requirement $\beta'^2 > 0$. Considering $x = \omega_t\omega_s$ it is possible to derive asymptotic limits for $R(\omega_t, \omega_s) \equiv R(x)$ in two regimes. For $x \to 1$ (i.e. near the threshold condition) $R(x) \to c\sigma_T/2(x-1)^{3/2}$, while for $x \gg 1$ (i.e. ultra-relativistic limit) $R \to \frac{3}{4} c\sigma_T \ln x/x$. An accurate and simple approximation which takes into account both regimes is given by

$$R(x) \approx 0.652 c\sigma_T \frac{x^2-1}{x^3} \ln(x)\, {\rm H}(x-1), \tag{A21}$$

where $H(x-1)$ is the Heaviside function. The approximation reproduces accurately the behaviour near the peak at $x_{\rm peak} \sim 3.7$ and over the range $1.3 < x < 10^4$ which usually is the most relevant during the calculations.

Arrival times and observed frequencies

The time when the observer receives the radiation produced at radius R is computed applying equation 26 in Nava et al. (2013), which has been derived under the assumption that the radiation is dominated by matter at $\cos\theta = \beta$ (in this case the Doppler factor is equal to Γ):

$$t = (1+z)\left[\int_0^R \frac{1-\beta_{\rm sh}}{\beta_{\rm sh} c} dr + \frac{R}{\Gamma^2(1+\beta)c}\right], \tag{A22}$$

where $\beta_{\rm sh}$ and β are the shock and fluid velocity, respectively, in units of c. This time results from the sum of a radial delay, that is, the difference between light travel time to radius R and shock expansion time to the same radius, and an angular delay for photons emitted from the same radius R but at $\cos\theta = \beta$ with respect to the line of sight.

Consequently, for the blueshift of the observed frequencies we adopt a Doppler factor $\delta = \Gamma$.

Jet geometry and jet break

The jet is assumed to be a cone with semi-aperture angle $\theta_{\rm jet}$ and top-hat geometry. The observer is assumed to be located along the jet axis. When $1/\Gamma \sim \theta_{\rm jet}$, the flux light curves steepens, due to geometrical effects and possibly to side-ways expansion. In our code we neglect the latter and consider only the geometrical effect.

For GRB 201216C, we find that a jet as narrow as $\theta_{\rm jet} \sim 1^\circ$ is needed to avoid overestimating the radio emission. Smaller jet opening angles (in the range 0.6°–1°) would still provide a very good fit of MAGIC, X-ray and optical observations and predict a lower flux in the radio band, where observations are available only at late times (>5 d).

Computation time and data modelling

The numerical code is computationally expensive. The time needed to compute one realization (i.e. infer spectra from radio to TeV energies and from a few seconds to several days) goes from about ten seconds to a few hours, depending mostly on the strength of the magnetic field (and hence on density and $\epsilon_{\rm B}$): short cooling times require shorter time steps in evolving the equation for particle evolution, and hence longer computation time.

To find a good modelling to the data, we thus start from a coarse grid of values for the parameters $E_{\rm k}$, $A_\star$ (or n_0), $\epsilon_{\rm e}$, $\epsilon_{\rm B}$, and p. The ranges investigated are reported in Table 2. After eliminating parts of the parameter space that give predictions completely inconsistent with observations, we repeated the simulations on narrower ranges of values and with a finer grid, until we found a good description of the data. We note that the values of Γ_0 and $\theta_{\rm jet}$ affect only the initial (before deceleration) and final part of the light curve. To save computation time, in our initial search of good solutions they are kept fixed to reasonable values and their values are adjusted only after good solutions are found, to improve the description of early-time data (before ∼300 s in the case of GRB 201216C) and of late-time data (i.e. to predict fluxes below the radio data, in case of GRB 201216).

[1]*Japanese MAGIC Group: Institute for Cosmic Ray Research (ICRR), The University of Tokyo, Kashiwa, 277–8582 Chiba, Japan*
[2]*Instituto de Astrofísica de Canarias and Departamento de Astrofísica, Universidad de La Laguna, E-38200 La Laguna, Tenerife, Spain*
[3]*Instituto de Astrofísica de Andalucía-CSIC, Glorieta de la Astronomía s/n, E-18008 Granada, Spain*
[4]*National Institute for Astrophysics (INAF), I-00136 Rome, Italy*
[5]*Università di Udine and INFN Trieste, I-33100 Udine, Italy*
[6]*International Center for Relativistic Astrophysics (ICRA), I-00185 Rome, Italy*
[7]*Max-Planck-Institut für Physik, D-80805 München, Germany*

[8]*Università di Padova and INFN, I-35131 Padova, Italy*
[9]*Institut de Física d'Altes Energies (IFAE), The Barcelona Institute of Science and Technology (BIST), E-08193 Bellaterra, Barcelona, Spain*
[10]*Technische Universität Dortmund, D-44221 Dortmund, Germany*
[11]*Croatian MAGIC Group: University of Zagreb, Faculty of Electrical Engineering and Computing (FER), 10000 Zagreb, Croatia*
[12]*IPARCOS Institute and EMFTEL Department, Universidad Complutense de Madrid, E-28040 Madrid, Spain*
[13]*Centro Brasileiro de Pesquisas Físicas (CBPF), 22290–180 URCA, Rio de Janeiro, Brazil*
[14]*Faculty of Physics and Applied Informatics, Department of Astrophysics, University of Lodz,, PL-90–236 Lodz, Poland*
[15]*Centro de Investigaciones Energéticas, Medioambientales y Tecnológicas, E-28040 Madrid, Spain*
[16]*ETH Zürich, CH-8093 Zürich, Switzerland*
[17]*Departament de Física, and CERES-IEEC, Universitat Autònoma de Barcelona, E-08193 Bellaterra, Spain*
[18]*Università di Pisa and INFN Pisa, I-56126 Pisa, Italy*
[19]*Universitat de Barcelona, ICCUB, IEEC-UB, E-08028 Barcelona, Spain*
[20]*Department for Physics and Technology, University of Bergen, Bjerknessenteret for klimaforskning, Allégaten 55, 5007 Bergen, Norway*
[21]*Institute for Astro- and Particle Physics, University of Innsbruck, A-6020 Innsbruck, Austria*
[22]*INFN MAGIC Group: INFN Sezione di Catania and Dipartimento di Fisica e Astronomia, University of Catania, I-95123 Catania, Italy*
[23]*Port d'Informació Científica (PIC), E-08193 Bellaterra, Barcelona, Spain*
[24]*INFN MAGIC Group: INFN Sezione di Torino and Università degli Studi di Torino, I-10125 Torino, Italy*
[25]*INFN MAGIC Group: INFN Sezione di Bari and Dipartimento Interateneo di Fisica dell'Università e del Politecnico di Bari, I-70125 Bari, Italy*
[26]*Croatian MAGIC Group: University of Rijeka, Faculty of Physics, 51000 Rijeka, Croatia*
[27]*Universität Würzburg, D-97074 Würzburg, Germany*
[28]*University of Geneva, Chemin d'Ecogia 16, CH-1290 Versoix, Switzerland*
[29]*Japanese MAGIC Group: Physics Program, Graduate School of Advanced Science and Engineering, Hiroshima University, 739–8526 Hiroshima, Japan*
[30]*Deutsches Elektronen-Synchrotron (DESY), D-15738 Zeuthen, Germany*
[31]*Armenian MAGIC Group: ICRANet-Armenia, 0019 Yerevan, Armenia*
[32]*Croatian MAGIC Group: University of Split, Faculty of Electrical Engineering, Mechanical Engineering and Naval Architecture (FESB), 21000 Split, Croatia*
[33]*Institute for Astro- and Particle Physics, University of Innsbruck, A-6020 Innsbruck, Austria*
[34]*Department of Physics, Croatian MAGIC Group: Josip Juraj Strossmayer University of Osijek, 31000 Osijek, Croatia*
[35]*Finnish MAGIC Group: Finnish Centre for Astronomy with ESO, University of Turku, FI-20014 Turku, Finland*
[36]*Department of Physics,, University of Oslo, 0371 Oslo, Norway*
[37]*Department of Physics, Japanese MAGIC Group: Tokai University, Hiratsuka, 259–1292 Kanagawa, Japan*
[38]*Dipartimento di Fisica, Università di Trieste, I-34127 Trieste, Italy*
[39]*Università di Siena and INFN Pisa, I-53100 Siena, Italy*
[40]*Saha Institute of Nuclear Physics, A CI of Homi Bhabha National Institute, Kolkata 700064, West Bengal, India*
[41]*Institute for Nuclear Research and Nuclear Energy, Bulgarian Academy of Sciences, BG-1784 Sofia, Bulgaria*
[42]*Finnish MAGIC Group: Space Physics and Astronomy Research Unit, University of Oulu, FI-90014 Oulu, Finland*
[43]*Japanese MAGIC Group: Chiba University, ICEHAP, 263–8522 Chiba, Japan*
[44]*Japanese MAGIC Group: Institute for Space-Earth Environmental Research and Kobayashi-Maskawa Institute for the Origin of Particles and the Universe, Nagoya University, 464–6801 Nagoya, Japan*
[45]*INAF Padova, I-35122 Padova PD, Italy*
[46]*Department of Physics, Japanese MAGIC Group: Kyoto University, 606–8502 Kyoto, Japan*
[47]*INFN MAGIC Group: INFN Sezione di Perugia, I-06123 Perugia, Italy*
[48]*INFN MAGIC Group: INFN Roma Tor Vergata, I-00133 Roma, Italy*
[49]*Department of Physics, Japanese MAGIC Group: Konan University, Kobe, Hyogo 658–8501, Japan*
[50]*Center for Astrophysics and Cosmology, University of Nova Gorica, Vipavska 11c, 5270 Ajdovščina, Slovenia*
[51]*Department of Physics, University of Bath, Claverton Down, Bath BA2 7AY, UK*
[52]*INAF-Osservatorio Astronomico di Brera, Via E. Bianchi, 46, I-23807 Merate LC, Italy*
[53]*European Space Agency, European Space Astronomy Centre, E-28692 Villanueva de la Canñada, Madrid, Spain*
[54]*Astrophysics Research Institute, Liverpool John Moores University, Liverpool Science Park IC2, 146 Brownlow Hill L3 5RF, UK*
[55]*Steward Observatory, University of Arizona, 933 North Cherry Avenue, Tucson, AZ 85721–0065, USA*

This paper has been typeset from a TEX/LATEX file prepared by the author.